Location of Seismic Signals Associated with Microearthquakes and Rockfalls on the Séchilienne Landslide, French Alps

by P. Lacroix and A. Helmstetter

Abstract   The Séchilienne rockslide, in the French Alps, has recently been instrumented with three seismic arrays. This network has recorded numerous rockfalls and local microearthquakes. Because the media is highly fractured, it is difficult to identify and pick first arrivals. Beam-forming methods were therefore used to locate these events. The method has been adapted to take into account the heterogeneity of seismic wave velocities. The location accuracy has been estimated to be about 50 m for epicenters by applying the method to calibration shots. Depth is less constrained due to uncertainties on the velocity model and due to the seismic network geometry.

This method of location has then been applied to rockfalls and microearthquakes. Most rockfalls initiate in the most active part of the rockslide called Les Ruines; the others are located on a recent eroded area aside from Les Ruines. The network also allows the estimation of the rockfall trajectory and propagation speed.

Finally, 55 microearthquakes have been located within two zones. Microearthquakes are located within the first 250 m below the surface. Most microearthquakes are located in Les Ruines, the most active part of the rockslide, where the velocity has increased from 0.5 m/yr in 1996 to 1.4 m/yr in 2008. These events are located close to three faults that delimit a mass of about 3.6 million m^3. Other events are located close to the summital scarp, in a zone moving at a few centimeters per year. The western part of the rockslide, which moves more slowly, did not produce any event large enough to be detected simultaneously by all stations. This seismic monitoring suggests that only a very small fraction of the deformation is released through seismic events.

Introduction

Assessing landslide hazard requires knowledge of its dynamics and internal structure. These characteristics are often difficult to estimate, especially for rockslides, because they often involve very fractured materials. Moreover, landslides may be subjected to different triggering factors, such as rainfall (Caine, 1980), earthquakes (Keefer, 1984), and atmospheric tides (Schulz et al., 2009) that impact their dynamics. To better understand landslide structure and the influence of external triggers on their dynamics, four landslides have been recently instrumented in the French Alps, as part of a project called Observatoire Muldisciplinaire des Instabilités de Versants (see the Data and Resources section). These landslides are instrumented with seismologic, displacement, meteorologic, and hydrologic sensors. The Séchilienne rockslide, situated 25 km southeast of Grenoble, is certainly the most instrumented among them, with geodetic instrumentation, geophysical investigations (Méric et al., 2005), drilling of a survey gallery and several boreholes, and seismic monitoring. This rockslide has been accelerating since 1996; the velocity of the most active zone has increased from 0.5 m/yr in 1996 up to 1.4 m/yr in 2008. The unstable slope threatens to dam the Romanche valley, with possible flooding of the Grenoble agglomeration (400,000 inhabitants) and the chemical industries of Jarrie situated downstream. This rockslide has been instrumented with different displacement sensors since the 1980s and was recently instrumented in May 2007 with a seismological network, consisting of three seismometer arrays (Helmstetter and Garambois, 2010).

Seismic networks are now commonly used to monitor landslides. Seismic monitoring has been used for detecting active faults (Spillmann et al., 2007), for assessing site effects (Del Gaudio, 2008), or for understanding the influence of triggering factors on rockslide dynamics (Helmstetter and Garambois, 2010). Seismic monitoring is of great interest for detecting rockfalls (Deparis et al., 2008; Moran et al., 2008; Vilajosana et al., 2008; Helmstetter and Garambois, 2010), debris flows (Burtin et al., 2009), and microseismicity precursors to large rockfall events (Amitrano et al., 2005).

The main goals of the Séchilienne seismic network are to detect and locate microearthquakes associated with fractures within the rockmass and to detect and characterize rockfalls. Helmstetter and Garambois (2010) have recently detected and classified seismic events (rockfalls and microearthquakes) from May 2007 until December 2009. Many rockfalls are triggered almost instantaneously following precipitation, and rockfall activity lasts for several days afterward. Precipitation also induces an acceleration of the rockslide. Velocity reaches its peak within a few days after rainfall and relaxes over a period of about one month.

Locating rockfalls and microearthquakes is important for better understanding their source and the mechanisms responsible for triggering. This is the main objective of the present work. Locating seismic events at Séchilienne is difficult because the rockmass is highly fractured. This results in highly heterogeneous seismic-wave velocities and significant attenuation of high-frequency waves, which makes picking first arrivals difficult. For these reasons, we use array

methods for locating rockfalls and microearthquakes. The method is first validated on calibration shots and synthetic signals, then compared with classical methods based on manual picking of first arrivals, and finally applied for locating natural seismic events recorded at Séchilienne.

Area of Study

The Séchilienne rockslide is situated 25 km southeast of Grenoble (French Alps) in the southern part of the Belledonne massif, and dominates the Romanche valley. It affects steep hercynian micashist slopes. The structure of the massif is characterized by N70°, N20°, and N140° faults formed during the hercynian orogenesis and north–south crushed areas like Les Ruines (Fig. 1) formed during the Alpine period. This specific structure delimits different areas of sliding. The summit part of Mont Sec (Fig. 1) exhibits a 20–40 m high scarp that initiated 6400 ± 1400 years ago, long after the end of the glacier retreat (13,300 years ago) (Le Roux
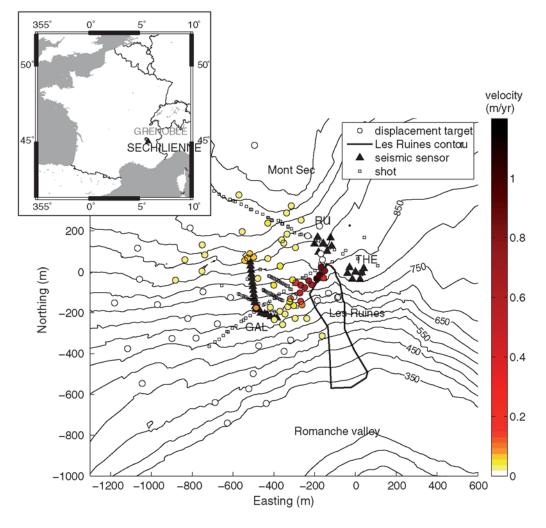

Figure 1.   Map of the Séchilienne rockslide. Filled circles show the position and velocity of displacement targets. Open squares show the location of shots realized for tomographic purpose. Seismometers are shown as black triangles. The color version of this figure is available only in the electronic edition.

et al., 2009). Its subsidence rate is now on the order of 1.8 cm/yr. The fastest moving area is situated at an elevation between 600 and 900 m and delimited by the N20°, N70°, and N140° faults (Fig. 1). The speed of this area has increased from 0.5 m/yr in 1996 up to 1.4 m/yr in 2008. The total volume of unconsolidated rockmass has been previously estimated between 3 and 20×10^6 m^3 (Giraud *et al.*, 1990), based on surface velocity and structural geology. A large uncertainty remains on this estimation due to the unknown rockslide geometry at depth.

The main risk associated with this rockslide is the damming of the Romanche River, which would flood the Grenoble agglomeration downstream in case of failure. Such a catastrophic rupture occurred in 1219 in the same valley. The presence of the Belledonne border fault less than 5 km away (Thouvenot *et al.*, 2003), with average recurrence time of 10,000 yrs for a magnitude 6 earthquake, increases the risk of the rockslide being triggered by an earthquake. For monitoring purposes, more than 100 displacement targets have been installed since 1985 and are measured several times per day with laser or radar (Evrard *et al.* 1990; Duranthon *et al.* 2003). A camera has also been installed recently to survey the motion within Les Ruines, where installation of targets is too dangerous. Also, a survey gallery has been drilled within the rockmass to map existing fractures and to better understand the structure of the rockslide. It is situated west of Les Ruines and is 240 m long. This horizontal gallery crosses several rigid moving blocks delimited by highly fractured zones. Unfortunately the gallery did not reach the base of the slide, and the presence of a sliding surface is still an open question.

Observations

Seismic Network

The network consists of three arrays of seismometers deployed around Les Ruines (Fig. 1). Two circular antennas, each consisting of six vertical-component 2-Hz sensors and one three-component sensor were first installed in May 2007. Array THE is located east of Les Ruines, and RUI is located just above Les Ruines. In April 2008, a third array of seismometers was installed west of Les Ruines and is referred to as station GAL. It is composed of 21 vertical-component 4.5-Hz sensors. Twelve among them were deployed in the 240-m long horizontal gallery. The nine others were first located on a line starting at the gallery entrance and going in the direction of Les Ruines, perpendicular to the direction of the gallery. In June 2009 these sensors were reinstalled to form a spiral above the gallery. This new configuration should improve event locations. The data are acquired continuously at 250 Hz for stations THE and RUI. Station GAL functions in trigger mode due to the large number of channels to limit the amount of data. Only events that were recorded simultaneously by all three stations are kept for analysis. Therefore, we analyze only those events occurring after the installation of station GAL in April 2008.

Source Classification

The network records different types of signals: local microearthquakes, earthquakes outside the rockslide, and rockfalls. Two seismic shot campaigns also occurred in June 2008 and January 2009. The June 2008 seismic profiles used 124 shots recorded by 48 geophones deployed along five different profiles, denoted PS1 to PS5 (Fig. 1). These shots were also recorded by our permanent network, except for shots of the profile PS5 that were not recorded by station THE. In January 2009, only the three short profiles PS2, PS3, and PS4 were realized. Unfortunately, the seismic campaigns were performed without a Global Positioning System, so the precise times of the shots are unknown.

In total, several thousands signals have been recorded by the network. A pseudoautomatic method has been developed for detecting and classifying events, as described in (Helmstetter and Garambois, 2010). Examples of signals are shown in Figure 2. Between 11 April 2008 and 9 June 2009, 341 events were detected by all stations. Among them, 16.1% were identified as local microearthquakes and 83% as rockfalls. A few events were rejected because their classification was too ambiguous.

Data Analysis

The location of seismic events on the Séchilienne rockslide is difficult because of the complex structure of the rockslide, which causes a large spatial variability of seismic wave velocities. The highly fractured nature of the landslide mass also strongly attenuates high-frequency waves. The recorded signals are thus weakly impulsive, and first arrivals are difficult to pick (Fig. 2). Also, because of the small distance between sensors and sources (< 1 km) and the low-frequency content of the signals, the P, S, and surface waves are mixed and difficult to identify.

Two methods can be used for locating seismic signals when picking first arrivals is impossible. First, beam-forming methods are based on intertrace correlation (e.g., Almendros *et al.*, 1999). The correlation coefficient provided by these methods is maximized to estimate the source location. These methods have been recently used for locating debris flows in the Himalaya (Burtin *et al.*, 2009), and microearthquakes in a glacier in the French Alps (Roux *et al.*, 2008). Second, polarization analysis methods (e.g., Jurkevics, 1988) allow the identification of different phases and an estimate of the direction of incoming waves. The source location can then be estimated by triangulating the source direction using at least two three-component seismometers. Because there are few three-components sensors in Séchilienne, we chose a beam-forming method to locate rockfalls and microearthquakes in this study.
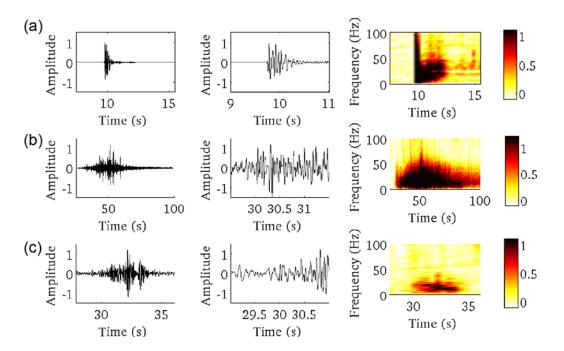
Figure 2. (Left) Seismic events recorded by sensor 1 of station THE, (middle) zoom over a 2-s window at the beginning of the signal, and (right) corresponding time–frequency diagram. All amplitudes have been normalized to the peak values. From top to bottom: (a) a shot, (b) a rockfall that occurred on 28 October 2008, (c) a local microearthquake that occurred on 29 October 2008. The color version of this figure is available only in the electronic edition.

Static Correction

Static corrections can be used to account for heterogeneities in the seismic wave velocities at stations, especially for local variations of velocity close to the sensors. The shot campaigns have been used to estimate residuals between estimated and modeled time delays. The station corrections are calculated in four steps:

- First, we manually pick the time τ_i^* of the first arrival for each trace and each shot. The measured time delay between traces i and j for a given shot is then defined as $\tau_{i,j}^* = \tau_i^* - \tau_j^*$.
- For each shot and for each station, we then invert for the velocity that minimizes the difference between the measured time delays $\tau_{i,j}^*$ and the theoretical time delays $\tau_{i,j} = \tau_i - \tau_j$ estimated by fixing the position of the source at its real location.
- For each shot, the static value for channel i between theoretical and measured time delays is given by $\langle \tau_{i,j} - \tau_{i,j}^* \rangle_j$, where $\langle \rangle_j$ is the average over channels j.
- The time correction for the channel i, τ_i^{static}, is then estimated by averaging this quantity over all shots.

These time corrections mirror the heterogeneity of seismic-wave velocity (Fig. 3). Negative time corrections correspond to larger local seismic wave velocity. They are observed for sensors inside the gallery and for the channels of RUI and THE that are further from Les Ruines. Positive time corrections correspond to low local seismic-wave velocity. They are observed for channels of GAL located outside the gallery because they are located in a deconsolidated area.

Beam-Forming Methods

We use a beam-forming method similar to the one used by Almendros *et al.* (1999) or Roux *et al.* (2008). The source location is estimated by maximizing the average intertrace correlation C after shifting traces in time by their travel time τ. The travel times are estimated for each sensor as a function of the source location (X, Y, Z) and sensor location (X_i, Y_i, Z_i), first assuming a uniform velocity V:

$$\tau_i = \frac{\sqrt{(X - X_i)^2 + (Y - Y_i)^2 + (Z - Z_i)^2}}{V}. \quad (1)$$

We then calculate the correlation coefficients $c_{i,j}$ between all couples of traces (x_i, x_j):

$$c_{i,j} = \frac{1}{\sigma_{x_i}\sigma_{x_j}} \int_{t_0-\delta_t/2}^{t_0+\delta_t/2} x_i(t - \tau_i + \tau_i^{\text{static}})x_j(t - \tau_j$$
$$+ \tau_j^{\text{static}})dt, \quad (2)$$

where t_0 is the time of signal maximum amplitude, δ_t is the time window duration, and σ_x is the standard deviation of x.

The inverse problem is then to find the source location (X, Y, Z) and velocity V that maximizes the average intertrace correlation

$$C(X, Y, Z, V) = \frac{1}{N^2} \sum_{i,j} c_{i,j}, \quad (3)$$

where N is the number of traces. The inversion of position and velocity is performed simultaneously, starting with a grid
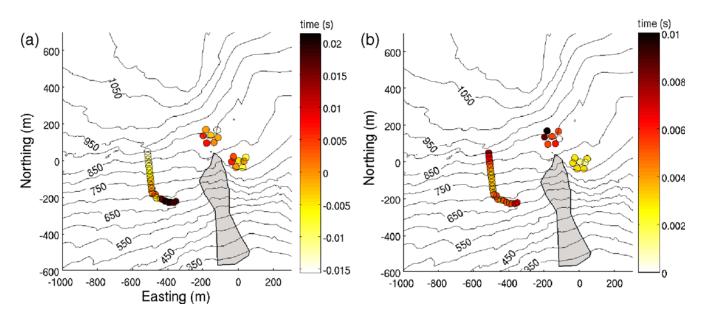
Figure 3. (a) Average value and (b) standard deviation of residuals between *P*-wave arrival times and theoretical time delays for shots. The color version of this figure is available only in the electronic edition.

search with a step of 50 m for *X,Y,* and *Z* and 1000 m/s for velocity. The depth is searched in the range between 0 and 500 m below the surface. This provides the initial solution for an optimization based on a Nelder–Mead sequential simplex algorithm. Each inversion consists of approximately 18,000 correlation coefficient calculations.

Because of the spatial configuration of the arrays and of the highly fractured and dispersive media, the intertrace correlation decreases rapidly with the intertrace distance. Therefore we adapt the method by applying a weight $w_{i,j}$ to the coefficient $c_{i,j}$ that depends on the distance $d_{i,j}$ between sensors i and j, expressed as a Lorentz function:

$$w_{i,j} = \frac{1}{1 + (d_{i,j}/d_{max})^2} \quad (4)$$

and

$$C(X, Y, Z, V) = \frac{\sum_{i,j} w_{i,j} c_{i,j}}{\sum_{i,j} w_{i,j}}, \quad (5)$$

where d_{max} is a parameter defining the correlation distance.

To take into account the heterogeneous medium, we use a different velocity for each array (THE, RUI, GAL). We also used a global velocity model consisting of a low-velocity layer on top of a homogeneous medium. This model was derived from manual picking of *P*-wave arrivals for the shots. The upper layer has a thickness of 36 m and a velocity $V_1 = 1285$ m/s, and the second infinite layer has a velocity $V_2 = 4101$ m/s. However, this model leads to substantial errors in shot location. Indeed the velocity and thickness of the upper layer is likely highly variable, so that a one-dimensional model is inaccurate. This test shows the three-dimensional nature of the landslide velocity.

Application to Shot Location

Our method is first applied to the 2008 and 2009 shot campaigns. A time window of $\delta_t = 1$ s is chosen around the signal peak time t_0. This value was chosen after a process of trial and error on the shots. The signal is then filtered below $f_{max} = 30$ Hz, and d_{max} is fixed to 50 m. These values minimize the shot location errors (Fig. 4). An example of the correlation *C* is represented for one shot in Figure 5. We tested different variants of the location method. For each shot, we compared the results obtained by using the same velocity for all three stations and by using a different velocity for each station. We also compared the results obtained by fixing the depth at the surface (Table 1) or by letting the depth vary
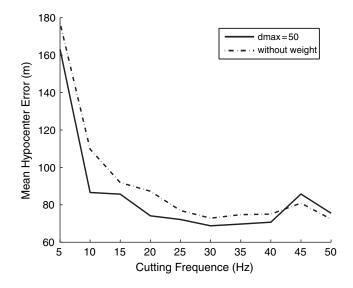

Figure 4. Mean location error for shots of June 2008 as a function of f_{max} for two runs with or without weight (d_{max}).
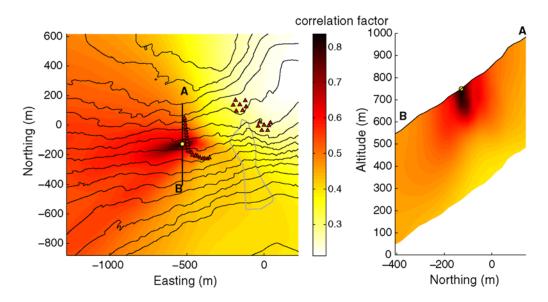
Figure 5. Correlation function C for a shot represented in map view (left) and in cross-section (right). The color version of this figure is available only in the electronic edition.

below the surface (Table 2). The results are represented in Figure 6. Errors between real and estimated locations are given in Table 1. This table provides an estimate of the error for all shots and for the shots situated inside the seismic network.

Horizontal Location Error. The results obtained with a constant velocity are relatively good for shots inside the network (around 60 m), but the average error increases significantly for shots outside the network. Using a different velocity for each station improves the location accuracy and provides an average horizontal error of about 50 m for events inside the network. However, in the northwestern part of our study area, source locations have a lower precision, mostly due to the configuration of the network. Indeed, these sources are outside the seismic network and aligned with stations RUI and THE.

In order to estimate the location accuracy, we define the area A where the average correlation C is larger than 97% of its peak value, C_{max}, in the plane parallel to the surface at the depth that maximizes C. The location accuracy l is then defined by $l = \sqrt{A}$. We compare this characteristic length l with the error ϵ between the real source and the estimated epicenter (Fig. 7). We see that l is roughly proportional to ϵ. A linear fit gives $l = 0.95\epsilon$, so that l provides a good estimate of the location error of epicenters.

Depth Error. In a second step, we have inverted for the depth in addition to the shot epicenter, in order to estimate the vertical location accuracy. Note that we imposed the source to be below the surface ($Z \geq 0$). The results are presented in Table 2. Thirty percent of the shots are located below the surface with the station-specific velocity. The average depth is 30 m, with a standard deviation of 52 m. This mean depth error is smaller than the mean horizontal error. However, its standard deviation is greater, indicating that the average depth error is less precisely estimated than the horizontal error. The smaller mean error at depth can thus be explained by two main reasons. First, regarding the large standard deviation of the depth error, the average depth error is probably calculated on too few samples. Second, the location process imposes the depth to be below the surface. The surface, however, is not a symmetry axis for the function $C(X, Y, Z)$ because of the topography and the presence of sensors at depth. As a consequence, many events are clustered at the surface, which reduce the depth error.

Table 1

Average Location Error and Standard Deviation for Shots by Fixing the Searched Depth at the Surface

| | Shot Campaign June 2008 | | Shot Campaign January 2009 | |
	All Shots	Inside Seismic Network	All Shots	Inside Seismic Network
Constant V	100 ± 94	61 ± 31	69 ± 46	59 ± 16
Station V	71 ± 50	52 ± 23	58 ± 46	50 ± 15

Statistics for location errors are given in meters. Location errors were estimated using either the same velocity for all sensors or a specific velocity for each station. The results are given for all shots and for those located inside the network.

Table 2
Same as Table 1 but Letting the Depth Vary below the Surface

| | Shot Campaign June 2008 | | | | Shot Campaign January 2009 | | | |
| | All Shots | | Inside | | All Shots | | Inside | |
	Horizontal	Depth	Horizontal	Depth	Horizontal	Depth	Horizontal	Depth
Constant V	84 ± 69	63 ± 79	67 ± 45	35 ± 45	75 ± 49	49 ± 60	62 ± 29	90 ± 55
Station V	61 ± 35	32 ± 54	50 ± 28	33 ± 44	65 ± 46	24 ± 50	53 ± 20	40 ± 48

The shape of the function $C(X, Y, Z)$ is elongated at depth (Fig. 5), which shows the low depth location precision. All shots located below the surface have a maximum correlation C_{max} very similar to the value $C_{Z=0}$ found by fixing the search depth at the surface. The difference $C_{max} - C_{Z=0}$ never exceeds 0.05 with a mean of 0.006 ± 0.01. Inverting for the source depth does not significantly change the epicenter location. The distance between epicenters located by inverting the depth or by fixing the source at the surface

is always smaller than 100 m, with a mean of 22 ± 30 m. We define the quantities z_{min} and z_{max} as the lower and upper depth limits where $C > 0.97 C_{max}$. For the shots, the average value is $z_{min} = 4 \pm 27$ m and $z_{max} = 147 \pm 119$ m.

This work shows that the location is fairly good for epicenters but not as good for depth. This is certainly caused by the geometry of the seismic network and by the heterogeneity of the seismic waves velocity. For natural sources, we will use the length l estimated from the correlation as
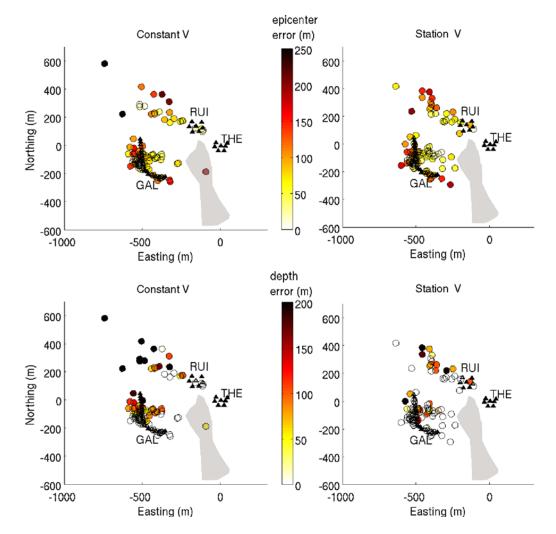

Figure 6. Location of shots (left) for a constant velocity and (right) for a station-specific velocity, estimated without fixing the depth at the surface. Top and bottom subplots represent epicenter and depth errors, respectively. The color version of this figure is available only in the electronic edition.
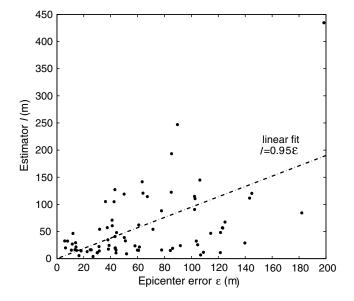
Figure 7. Epicenter location error ϵ versus the distance l estimated from the area where $C > 0.97 C_{\max}$. The dash-dot line represents the linear fit between these two quantities.

an estimate of the location accuracy for epicenters. For hypocenters, the range of depths where the correlation is larger than 97% of $C_{\max}$ can also provide an estimate of the location error.

Sources of Errors. We have tested our location method on synthetic signals, generated in a uniform media and composed of P and S waves overlapping in time and having the same frequency content as natural signals. The source was either isotropic (same amplitude for each trace or amplitude and decreasing with distance from the source) or anisotropic (applying a scaling factor varying as the cosine of the azimuth of the source to each trace). Noise of varying amplitude was added to each trace, obtained by band-pass filtering Brownian noise. Location accuracy is of the order of 30 m inside the network for signal-to-noise ratio (SNR) such that $C_{\max} > 0.5$, but the error is much larger outside the network.

The location is thus a little more accurate for synthetics than for real events. This could be due to seismic wave heterogeneity, which is not included in the synthetics that were generated using a uniform velocity. Seismic wave heterogeneity is only partially accounted for in our location method by using static corrections and station-specific velocity. Synthetic tests show that the location is more accurate when the intertrace correlation is larger. Therefore, when locating seismic signals recorded at Séchilienne, we will only select events with $C_{\max} > 0.5$.

We have also compared the method with location based on manually picking first arrivals for the 67 shots for which first arrivals are easily identified. The location is done by inverting the source location (X, Y, Z) and the velocity (V) that minimize the sum of the residual between picked

and modeled time delays. As previously described in this paper, this inversion is done through a grid search in X, Y, Z, and V dimensions that provides the initialization for an optimization. The epicenter error is 95 ± 67 m inside the array, around twice the error found with our method. The depth error is 37 ± 49 m, similar to our method. Cross-correlation method thus provides better location results than picking of first arrivals.

Rockfall Location

Rockfall signals are composed of a succession of block impacts, which move downward with time. Therefore, the rockfall location is done using the beginning of the signal in order to locate the position of the first impacts. The time window used is 1 s long and centered on the first impact identified with SNR greater than 3. The signal is filtered below 30 Hz. Two location steps are performed; the depth is first fixed at the surface, and, second, it is allowed to vary freely below the surface. The goal of this second step is to estimate the depth location error on natural events. This second step shows that the rockfall depth is estimated to be smaller than 4 m for 78% of events. The other 22% of rockfalls with depths estimated deeper than 4 m have epicenter locations close to that estimated by fixing the depth at the surface.

The $z_{\min}$ and $z_{\max}$ distribution is shown in Figure 8. This distribution is different from the one found for the shots. In particular, the $z_{\min} - z_{\max}$ range is greater, indicating that the rockfall depths are poorly constrained. However, the mean depth error is 22 ± 51 m, smaller than the shot mean depth error. The location accuracy of epicenters is estimated by l, calculated from the correlation map. The location of rockfalls and their precision is shown in Figure 9. This map shows two main areas of rockfall initiation: the main one in the upper part of Les Ruines, comprising 80% of the rockfalls, and another between station GAL and Les Ruines. This second area corresponds to a zone of recent erosion, which is easily seen on aerial images.

In order to analyze rockfall propagation, we then try to locate each impact identified on the rockfall signal with SNR greater than 3 (Fig. 10). The measured rockfall speed is then calculated from the position of successive impacts and is found to vary between 36 m/s for the beginning of the signal and 50 m/s at the bottom of the slope. Monitoring rockfall propagation has previously been undertaken by Vilajosana *et al.* (2008). These authors used two three-component seismometers to estimate the direction of the source from the wave polarization during a rockfall. The rockfall location is then found by triangulating the two directions from the two seismometers. However, the wave identification through polarization estimation can be difficult for moving sources in complex media, as the resulting polarization is a superimposition of different waves coming from different sources delayed in time. The method presented here is thus a good alternative to the polarization methods. A sensor at the bottom of the slope, however, would be useful to better
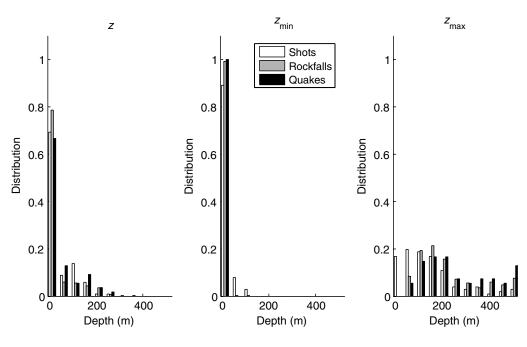
Figure 8. (Left) Distribution of depth, (middle) z_{min}, and (right) z_{max} for the different types of events. White, shots; gray, rockfalls; black, microearthquakes.

estimate the trajectory, as the location precision decreases with increasing distance from the network.

Microearthquakes

Location of Microearthquakes

The microearthquakes are located using the same method. The source locations and their estimated errors are mapped in Figure 9. The correlation for microearthquakes is higher (0.75 ± 0.08) than for rockfalls (0.65 ± 0.08), suggesting that the method works better for discrete sources like earthquakes. The smaller correlation for rockfalls may

be due to the superposition of waves from different sources or to the frequency content of rockfalls, which often have less low-frequency energy than do earthquakes. For comparison, the correlation coefficients obtained for the shots is 0.71 ± 0.06.

The estimated depths are found to vary within the upper 250 m, with most events situated at the surface (Fig. 11). The volume where the correlation is close to its maximum value is elongated in depth, and thus the confidence in the estimated depth is rather low. However, two clues suggest the existence of deeper events: the fraction of microearthquakes found at the surface (65%) is lower than for rockfalls (78%)
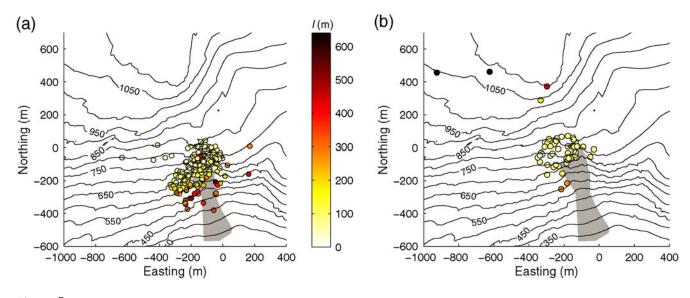

Figure 9. Location of natural events: (a) rockfalls; (b) microearthquakes. The location error is provided by the estimate l. The color version of this figure is available only in the electronic edition.
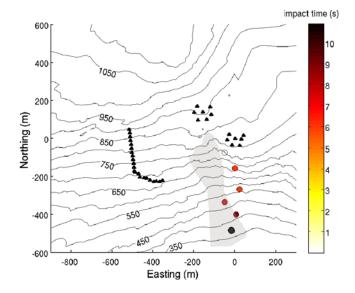
Figure 10. Location of impacts during the propagation of a rockfall that occurred on 6 June 2008. The color version of this figure is available only in the electronic edition.

and shots (70%), and, on average, z_{max} is greater for earthquakes than for other events (Fig. 8).

The spatial distribution of microseismicity reveals two seismically active areas. Most microearthquakes are located in the fast-moving area located in the upper part of Les Ruines (Fig. 1). These events seem to delineate the contour of the most active zone (Fig. 11). Their locations are coincident with the position of three faults: a N°140 fault on its eastern side, a N°20 fault north of this area, and several N°70 faults on the southern part of this area (Fig. 11). These three lineaments delimit the fast-moving block in the upper part of

Les Ruines. A previous study (Giraud *et al.*, 1990), based on the velocity profile inside the gallery, has suggested that the movement at Séchilienne is controlled by parallel toppling blocks delimited by vertical faults.

The second zone is situated in the upper part of the rockslide. The location precision of these events is low due to their situation outside the network. However, they seem to be situated on the active Mont Sec scarp shown in Figure 11. Cosmogenic studies have shown that this scarp has been moving for ≈6400 yrs with vertical velocities varying between 0.3 and 1.8 cm/yr (Le Roux *et al.*, 2009). This motion may be expressed by seismic activity due to fracturing or sliding along the scarp. In the future, longer duration records will allow a better quantification of this seismicity. The question still remains about the presence of a sliding surface on the Séchilienne rockslide.

The small number of seismic events and their limited depth accuracy make it difficult to identify the geometry of the unstable zone. Nevertheless, the location of microearthquakes suggests that the active deformation occurs within the upper 250 m. Interpolating through the microearthquakes situated at depth provides a volume ≈3.6×10^6 m^3 (Fig. 11). A previous study has estimated the volume of the most active zone to about 3×10^6 m^3, based on surface velocity and structural observations (Giraud *et al.*, 1990), which is consistent with our seismicity-based estimate.

Magnitude

We estimate the magnitudes from the peak amplitude A of each event and the distance R from the network, using the amplitude–magnitude relation of Hanks and Kanamori (1979),
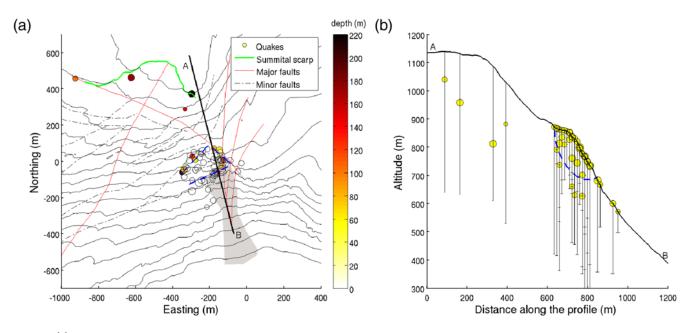

Figure 11. (a) Location of microearthquakes on a geological map. Microearthquakes are represented with circles sized by their magnitude. (b) Sources projected on the profile A–B. The dashed line represents the limit of the unstable area as estimated from the seismicity. The color version of this figure is available only in the electronic edition.

$$M = \frac{2}{3}\log(RA) + K, \qquad (6)$$

where K is a constant depending on site effects, seismic waves velocity, rock density, and other fixed corrections. Seismic velocity and rock density are not precisely known and are very heterogeneous at Séchilienne. For this reason, and also to correct for site effects, we have calibrated the magnitude relation using earthquakes that have also been detected by the regional SISMALP network (Thouvenot *et al.*, 2003).

We filter the signal below 30 Hz and define the long-period amplitude A as the maximum of the signal for each source and each sensor. The magnitude is found by averaging all the magnitudes of the different sensors, after removing the sensors with very different values (more than two standard deviations from the average magnitude). The difference between the real magnitude and the magnitude found with the Séchilienne network is computed for each sensor and each earthquake detected by SISMALP. The mean difference provides the constant K for each sensor. This constant is estimated with a standard deviation of ± 0.24.

The microearthquake magnitudes range from -1.1 to 0.1, with a standard deviation between sensors of ± 0.2. The magnitude distribution is shown in Figure 12. These magnitudes are comparable to the ones found on the Randa landslide (Spillmann *et al.*, 2007). The completeness threshold of the network is $M -0.9$. Despite the small number of events, this distribution follows a Gutenberg–Richter law with $b = 1.6$. This value is higher than the classical value ($b = 1$) found in tectonically active areas and can be explained by the large heterogeneities of the landslide materials (Mogi, 1962).

We can estimate the proportion of energy released through seismic events by comparing the cumulative moment of microearthquakes and the total moment M_0
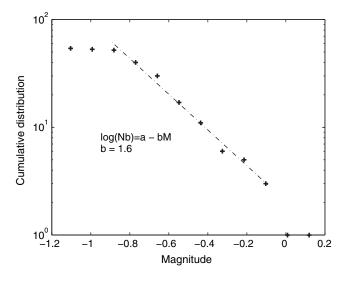
released by the deformation of the most active area only. M_0 is given by $M_0 = \mu SD$, where μ is the rigidity (in GPa), S is the sliding area ($S \approx 30000$ m^2) of the most active zone, and D is the displacement per year ($D \approx 1.4$ m). The rigidity for metamorphic rocks is of the order of 20 GPa. The moment released by this deformation is $M_0 \approx 10^{22}$ dyne cm, which is equivalent to an earthquake of magnitude 3.9. This number is far more important than the seismic moment 1.8×10^{16} dyne cm of the largest event recorded.

For most earthquake catalogs, the magnitude distribution obeys the Gutenberg–Richter law with $b < 1.5$, and therefore the cumulated seismic moment release is driven by the largest earthquakes (Bird and Kagan, 2004). In our case, the b value is 1.6; therefore, there are many more small events than larger ones, and the small undetected events collectively dominate the deformation. The total seismic moment released per year (in dyne cm) for all earthquakes of magnitude between $m_{\min}$ and $m_{\max}$ is given by (Hanks and Kanamori, 1979):

$$M_0 = \int_{m_{\min}}^{m_{\max}} P(m)10^{1.5m+16.1}dm, \qquad (7)$$

where $P(m) \approx 7 \times 10^{-1.6m}$ is the number of events with magnitude m per year estimated from Figure 12, corresponding to about two $m \geq 0$ earthquakes per year. Replacing $P(m)$ by its expression in equation (7), we get

$$M_0 \approx 4 \times 10^{17}(10^{-0.1m_{\min}} - 10^{-0.1m_{\max}}). \qquad (8)$$

This expression diverges very slowly for small magnitudes and saturates with $m_{\max}$. Even when choosing a very large magnitude interval $m_{\min} = -14$ (rupture length of about 1 μm) and $m_{\max} = 5$ (rupture length equal to the rockslide area), we obtain $M_0 \approx 10^{19}$ dyne cm, about 0.1% of the seismic moment release due to the slope movement. Therefore, most of the deformation of the rockslide is aseismic, even when accounting for small undetected earthquakes.

Conclusion

We have developed a method for locating seismic signals based on intercorrelation of signals at different sensors. This method is well adapted to locate emergent signals and propagating sources, which makes it a powerful tool for monitoring rockfall propagation and for locating emergent low-frequency signals generated by microearthquakes. This method provides source location with a precision of about 50 m for events inside the seismic network. The location error can be estimated from the contour of the volume inside which the correlation is close to its maximum value. In order to account for the heterogeneity of seismic waves velocities, we have used calibration shots to estimate station corrections, and we have also used a specific velocity for each array and for each event. We have compared our method with traditional location methods based on manual picking of P-wave arrival using calibration shots, and our method

Figure 12. Cumulative magnitude distribution for microearthquakes.

is found to work better. In addition, it can be applied to moving sources and is fully automatic.

The seismic monitoring of Séchilienne shows an intense rockfall activity within the area of Les Ruines and also in a more recently eroded area outside of Les Ruines. Unfortunately, the rock volumes have not yet been estimated. A video camera has been recently installed in front of Les Ruines for better rockfall monitoring, which will be used in the future for estimating volumes of individual rockfalls and calibrating seismic signals.

Microearthquakes are located in two areas. During the first 14 months of the seismic monitoring, 7% of earthquakes were located close to the Mont Sec scarp, at the top of the rockslide. This zone is affected by active faulting. Despite the relative old initiation of this scarp ($\approx$6400 yrs ago), this area still presents some microseismic activity.

The fastest moving zone in the upper part of Les Ruines is the most seismically active, with 51 microearthquakes recorded in 14 months. The velocity of this area reaches more than 1.4 m/yr (Pothérat and Alfonsi, 2001). These microearthquakes delimit a block of about 3 ha, with a mean depth of 120 m. The earthquake locations follow lineaments corresponding to three families of faults of orientation N°20, N°70, and N°140. Taking the active faults as the limit of the unstable block provides an estimate of the unstable volume of $\approx$3.6 × 10^6 m^3. This volume is smaller than the minimum volume required to dam the valley and create a lake, which has been estimated to be 5 × 10^6 m^3. Nevertheless, the failure of a 3.6 × 10^6 m^3 block would produce considerable damage to infrastructures in the downhill valley. Moreover the dynamic behavior of the whole landslide after this block failure is highly unknown.

The other parts of the rockslide are found to move without any recordable seismicity. Longer period of seismic monitoring should allow a better definition of the seismically active parts of the rockslide, especially at depth, and a better understanding of the link between surface motion, microseismicity, and triggering factors.

Data and Resources

All seismic data have been acquired by the Observatoire Multidisciplinaire des Instabilités de Versants (OMIV) project, and data are available online at http://www-lgit .obs.ujf-grenoble.fr/observations/omiv. The SISMALP earthquake catalog has been provided by François Thouvenot. Centre d'Etudes Techniques de l'Equipement (CETE) provided the displacement data.

Acknowledgments

References

Almendros, J., J. M. Ibanez, G. Alguacil, and E. Del Pezzo (1999). Array analysis using circular-wave-front geometry: An application to locate the nearby seismo-volcanic source, *Geophys. J. Int.* **136,** 159–170.

Amitrano, D., J. R. Grasso, and G. Senfaute (2005). Seismic precursory patterns before a cliff collapse and critical point phenomena, *Geophys. Res. Let.* **32** no. 8, L08314.1–L08314.5, doi 10.1029/2004GL022270.

Bird, P., and Y. Y. Kagan (2004). Plate-tectonic analysis of shallow seismicity: Apparent boundary width, beta, corner magnitude, coupled lithosphere thickness, and coupling in seven tectonic settings, *Bull. Seismol. Soc. Am.* **94,** 2380–2399.

Burtin, A., L. Bollinger, R. Cattin, J. Vergne, and J. L. Nabelek (2009). Spatiotemporal sequence of Himalayan debris flow from analysis of high-frequency seismic noise, *J. Geophys. Res.* **114,** no. F04009, doi 10.1029/2008JF001198.

Caine, N. (1980). The rainfall intensity-duration control of shallow landslides and debris flows, *Geogr. Ann. Phys. Geogr.* **62A,** 23–27.

Del Gaudio, V., S. Coccia, J. Wasowski, M. Gallipoli, and M. Mucciarelli (2008). Detection of directivity in seismic site response from microtremor spectral analysis, *Nat. Hazards Earth Syst. Sci.* **8,** 751–762.

Deparis, J. D., F. Jongmans, F. Cotton, L. Baillet, F. Thouvenot, and D. Hantz (2008). Analysis of rock-fall seismograms in the western Alps, *Bull. Seismol. Soc. America* **98,** no. 4, 1781–1796.

Duranthon, J. P., L. Effendiantz, M. Memier, and I. Previtali (2003). Apport des méthodes topographiques et topométriques au suivi du versant rocheux instable des ruines de Séchilienne, *Association francaise de topographie* **94,** 31–38.

Evrard, H., T. Gouin, A. Benoit, and J. P. Duranthon (1990). Séchilienne, Risques majeurs d'éboulements en masse: Point sur la surveillance du site, *Bull. Liaison Lab. Ponts Chauss* **165,** 7–16.

Giraud, A., L. Rochet, and P. Antoine (1990). Processes of slope failure in cristallophyllian formations, *Eng. Geol.* **29,** 241–253.

Hanks, T. C., and H. Kanamori (1979). Moment magnitude scale, *J. Geophys. Res.* **84,** 2348–2350.

Helmstetter, A., and S. Garambois (2010). Seismic monitoring of Séchilienne rockslide (French Alps): Analysis of seismic signals and their correlation with rainfalls, *J. Geophys. Res.* **115,** no. F03016, doi 10.1029/2009JF001532.

Jurkevics, A. (1988). Polarization analysis of three-component array data, *Bull. Seismol. Soc. Am.* **785,** 1725–1743.

Keefer, D. K. (1984). Landslides caused by earthquakes, *Geol. Soc. Am. Bull.* **95,** 406–421.

Le Roux, O., S. Schwartz, J. F. Gamond, D. Jongmans, D. Bourles, R. Braucher, W. Mahaney, J. Carcaillet, and L. Leanni (2009). CRE dating on the head scarp of a major landslide (Séchilienne, French Alps), age constraints on Holocene kinematics, *Earth Planet. Sci. Lett.* **28,** no. 1–4, 236–245.

Méric, O., S. Garambois, D. Jongmans, M. Wathelet, J.-L. Chatelain, and J.-M. Vengeon (2005). Application of geophysical methods for the investigation of the large gravitational mass movement of Séchilienne, France, *Can. Geotech. J.* **42,** 1105–1115.

Mogi, K. (1962). Magnitude-frequency relation for elastic shocks accompanying fractures of various materials and some related problems in earthquakes, *Bull. Earthq. Res. Inst., Univ. Tokyo* **40,** 831–853.

Moran, S. C., R. S. Matoza, M. A. Garces, M. A. H. Hedlin, D. Bowers, W. E. Scott, D. R. Sherrod, and J. W. Vallance (2008). Seismic and acoustic recordings of an unusually large rockfall at Mount St. Helens, Washington, *Geophys. Res. Lett.* **35,** doi 10.1029/2008GL035176.

Pothérat, P., and P. Alfonsi (2001). Les mouvements de versant de Séchilienne (Isère). Prise en compte de l'héritage structural pour leur simulation numérique, *Revue Francaise de Géotechnique* **95,** 117–131.

Roux, P.-F., D. Marsan, J.-P. Metaxian, G. O'Brien, and L. Moreau (2008). Microseismic activity within a serac zone in an alpine glacier (Glacier d'Argentière, Mont Blanc, France), *J. Glaciol.* **54,** 157–168, 184.

Schulz, W. H., J. W. Kean, and G. Wang (2009). Landslide movement in southwest Colorado triggered by atmospheric tides, *Nature Geosci.* **2,** 863–866.

Spillmann, T., H. Maurer, A. G. Green, B. Heincke, H. Willenberg, and D. Husen (2007). Microseismic investigation of an unstable mountain slope in the Swiss Alps, *J. Geophys. Res.* **112,** no. B07301, doi 10.1029/2006JB004723.

Thouvenot, F., J. Fréchet, L. Jenatton, and J. F. Gamond (2003). The Belledonne border fault: Identification of an active seismic strike-slip fault in the western Alps. *Geophys. J. Int.* **155,** 174–192.

Vilajosana, I., E. Surinach, A. Abellan, G. Khazaradze, D. Garcia, and J. Llosa (2008). Rockfall induced seismic signals: Case study in Montserrat, Catalonia, *Nat. Hazards Earth Syst. Sci.* **8,** 805–812.

Laboratoire de Géophysique Interne et Tectonophysique
Centre National de la Recherche Scientifique
Université Joseph Fourier
F-38041 Grenoble, France
pascal.lacroix@obs.ujf-grenoble.fr